# Many-electron calculations of the phase stability of $ZrO_2$ polymorphs

Wernfried Mayr-Schmölzer,[1,*] Jakub Planer,[1] Josef Redinger,[1] Andreas Grüneis,[2] and Florian Mittendorfer[1]
[1]*Center for Computational Materials Science, Vienna University of Technology, Wiedner Hauptstrasse 8-10, 1040 Vienna, Austria*
[2]*Institute for Theoretical Physics, Vienna University of Technology, Wiedner Hauptstrasse 8-10, 1040 Vienna, Austria*

(Received 23 December 2019; revised 30 June 2020; accepted 16 October 2020; published 11 December 2020)

Zirconia ($ZrO_2$) has been well studied experimentally for decades, but still poses a severe challenge for computational approaches. We present thorough many-electron benchmark calculations within the random-phase approximation framework of the phase stabilities of the most common $ZrO_2$ phases and assess the performance of various density functional theory (DFT) and beyond-DFT methods. We find that the commonly used DFT and hybrid functionals strongly overestimate both the energetic differences of the common phases and the stability of two metastable phases. The many-electron calculations offer a significantly improved description of the predicted bulk properties, especially of the bulk modulus $B_0$. On the DFT level, the van der Waals corrected meta-generalized-gradient approximation (SCAN-rVV10) provides much better agreement with the experimental values than other (semi)local and hybrid approaches.

DOI: 10.1103/PhysRevResearch.2.043361

## I. INTRODUCTION

Zirconia ($ZrO_2$) is a versatile material used in many technological applications, like catalysis, gas sensors, or solid oxide fuel cells. It has therefore been extensively studied for decades, exposing a complicated phase diagram. It is a very good insulator with a large band gap of $>5.8$ eV [1] and a large bulk modulus of $\approx$200 GPa, but its behavior under tensile stress depends on its crystallographic structure [2]. More recently, ferroelectricity was discovered in $ZrO_2$- and related $HfO_2$-based materials [3–6]. While an estimated electric field of 1 MV/cm is needed to activate the phase transition to the polar orthorhombic phase of pure $ZrO_2$, mixed $Hf_{0.5}Zr_{0.5}O_2$ (HZO) materials are predicted to be ferroelectric at small grain sizes [6] or as thin HZO films [5].

The ground state of zirconia crystallizes in a monoclinic [space group (SG) $P2_1/c$] crystal symmetry [7]. At elevated temperatures phase transitions are observed, first to a tetragonal (SG $P4_2/nmc$) phase which is stable between 1270 and 1370 K [8,9], followed by a cubic (SG $Fm\bar{3}m$) phase at about 2650 K [8]. Furthermore, three orthorhombic phases exist: the orthorhombic I phase (SG *Pbca*) and the orthorhombic II phase (SG *Pnma*) occur at transition pressures of 4–12 GPa [10,11] and $>20$ GPa [11], respectively. The third orthorhombic phase is polar ($f$ phase, $Pca2_1$) [12], and can be stabilized by cooling down tetragonal $ZrO_2$ from about 2000 to 30 K. The cubic yttrium doped $ZrO_2$ is commonly used in technological applications, and undoped $ZrO_2$ films have been studied in recent years as a very well-defined model system. For example, ultrathin films of cubic $ZrO_2$ with a low amount of surface defects can be easily grown via the oxidation of a suitable metal alloy such as $Pt_3Zr$ [13–15] or $Pd_3Zr$ [16].

In recent decades, the bulk phases of $ZrO_2$ were studied extensively using density functional theory (DFT) [6,17,18]. DFT functionals like the Perdew-Burke-Ernzerhof (PBE) functional generally yield the correct order of stability, while the lattice parameters and bulk modulus are still largely over- and underestimated, respectively. Additionally, the calculated band gap of about 3.5 eV falls short of the large experimental value of $>5.8$ eV. Due to the computational cost, the assessment of the dynamics of the structural transitions of various $ZrO_2$ phases was restricted to the DFT level [9,19–21]. While the results seem to agree well with experimental observation, the deformations of the $ZrO_2$ lattice during the phase transition have led to the discovery of various additional metastable phases, all of which have yet to be corroborated by experiment. In a recent study based on diffusion Monte Carlo simulations [22], Shin and coworkers find good agreement between their predicted lattice parameters and experimental values, but a rather large deviation for the predicted bulk moduli of the monoclinic and tetragonal phases.

The importance of systematic benchmark calculations for materials modeling was discussed in a recent review by Lejaeghere *et al.* [23]. In this work we present a thorough assessment of the performance of DFT and many-electron random-phase approximation (RPA) approaches with respect to the order of stability of the thermally induced $ZrO_2$ phases and their physical properties. We discuss the shortcomings of the PBE and HSE06 functionals in the description of metastable phases and show the importance of zero-point vibrational energy corrections for this complex system.

## II. COMPUTATIONAL METHODS

The calculations were performed using the Vienna *Ab initio* Simulation Package (VASP), a projector augmented plane-wave basis code [24]. The electronic interactions were

*wms@cms.tuwien.ac.at

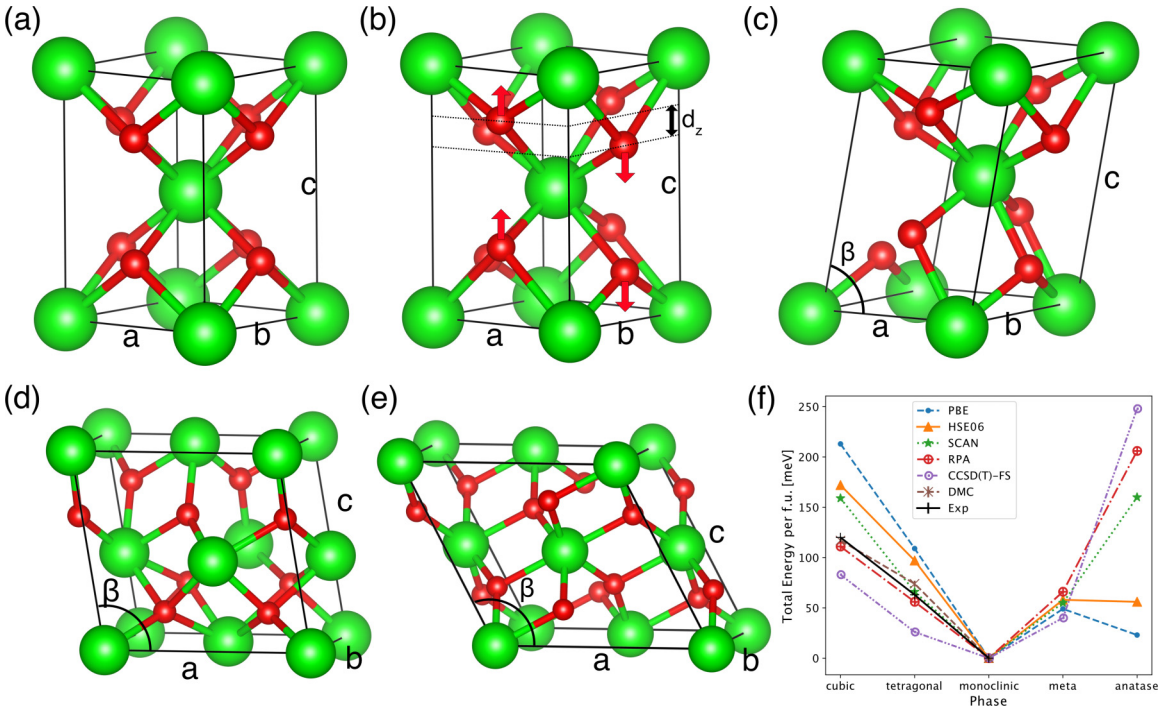


FIG. 1. (a)–(e) Cubic, tetragonal, metamonoclinic, monoclinic, and anatase phases. Zr and O atoms are colored green and red, respectively. (f) Total energy differences per formula unit of the five phases calculated with selected functionals.

described within the framework of DFT using the PBE [25], the SCAN meta-generalized-gradient approximation (metaGGA) [26], and the hybrid HSE06 exchange correlation (xc) functional [27]. Additionally, van der Waals (vdW) corrections were included for the PBE and HSE06 functionals using Grimme's D3 method [28]. The revised Vydrov–van Voorhis nonlocal correlation functional [29] was finally used to take long-range van der Waals interactions within the SCAN metaGGA functional into account [30]. Scalar relativistic effects are already included in the used pseudopotentials, and fully relativistic treatment at the PBE level shows changes of the energy differences between phases of below 1 meV. Other light oxides like SnO exhibit a similarly negligible influence from including spin-orbit coupling for the valence states [31,32]. The direct second-order Møller-Plesset (dMP2) and RPA calculations were performed using an efficient low-scaling algorithm [33]. The forces at the RPA levels were evaluated as the first derivative of the energy with respect to the Green's function [34]. For all DFT and hybrid calculations both shape and internal coordinates of the unit cells were fully relaxed. The non-self-consistent total energy calculations using the dMP2 method and the RPA were performed based on PBE-optimized cell shapes and relaxed RPA internal coordinates. To achieve convergence of the plane-wave basis set, the energy cutoff was set to 600 eV for the DFT and hybrid calculations and to 550 eV for the dMP2 and RPA simulations. Γ-centered $6 \times 6 \times 6$ and $4 \times 4 \times 4$ $k$-point grids were used to sample the Brillouin zone. The model cells of phases were set up using two (cubic, tetragonal, and metamonoclinic phases) or four (monoclinic, anatase) formula units (see Fig. 1). The cubic, tetragonal, and metamonoclinic unit cells were doubled to encompass four formula units to facilitate the $k$-point convergence for the dMP2 and RPA calculations.

To determine the equilibrium volume, total energy calculations were performed at different volumes and the results were fitted to a Birch-Murnaghan equation of state [35] which allows the direct evaluation of the bulk modulus $B_0$. For a subset of phases where experimental data have been published, the elastic constants $C_{ij}$ were computed using the finite difference method. Here, the forces and elastic constants are derived from the Hessian matrix which is determined by symmetry equivalent displacements of each ion in the direction of the Cartesian coordinates. The elastic tensor was then derived from the strain-stress relationship [36] by performing six finite distortions of the lattice. From the elastic constants the bulk modulus $B_v$ in the Voight approximation can be directly evaluated. The zero-point vibrational energies were evaluated with the PHONOPY [37] package using $2 \times 2 \times 2$ unit cells and otherwise identical computational settings.

Additional MP2 and coupled cluster calculations were performed using the the coupled cluster for solids (CC4S) [38] code employing an automated tensor contraction framework (CTF) [39] interfaced to VASP. In these calculations, we use natural orbitals to achieve a compact approximation to the virtual orbital manifold [40]. Due to the computational cost involved, only unit cells containing 16 O and 8 Zr atoms were used. Finite size errors in the MP2 and CCSD calculations were reduced with a recently proposed correction [41] (-FS) and by adding the difference between dMP2-FS and fully $k$-point converged dMP2 ($+\Delta$).

## III. RESULTS AND DISCUSSION

In the present study we computed the optimal lattice parameters for the monoclinic ground state, the two high temperature tetragonal and cubic phases, and the two

TABLE I. Total energy differences per formula unit (f.u.) of the cubic (c), tetragonal (t), metamonoclinic (meta), monoclinic (m), and anatase (a) phases in meV referenced to the monoclinic ground state. Experimental enthalpy differences were obtained at the respective phase transition temperature in Ref [42].

| | c | t | meta | m | a |
|---|---|---|---|---|---|
| | | (meV/formula unit) | | | |
| LDA | 93 | 48 | 61 | 0 | 252 |
| PBE | 213 | 109 | 49 | 0 | 23 |
| PBE-D3 | 194 | 108 | 54 | 0 | 105 |
| HSE06 | 172 | 97 | 58 | 0 | 56 |
| HSE06-D3 | 152 | 92 | 61 | 0 | 154 |
| SCAN | 159 | 66 | 55 | 0 | 160 |
| SCAN-rVV10 | 137 | 52 | 56 | 0 | 217 |
| dMP2 | 121 | 56 | 47 | 0 | 240 |
| RPA | 111 | 56 | 66 | 0 | 206 |
| MP2-FS+Δ | 98 | 39 | 57 | 0 | 244 |
| CCSD-FS+Δ | 70 | 32 | 50 | 0 | 224 |
| CCSD(T)-FS+Δ | 83 | 26 | 40 | 0 | 248 |
| DMC [22] | 110±7 | 70±4 | | 0 | |
| Expt. [42] | 120 | 63 | | 0 | |

distorted metamonoclinic and anatase phases (see Fig. 1 for the complete data). The metamonoclinic phase introduced by Thomas *et al.* [19] is a metastable structure along a transition path involving the change of the monoclinic shear plane between two isosymmetric monoclinic phases. Chen *et al.* [21] found a closely related structure identified as an orthorhombic $P2_12_12_1$ phase after accounting for anharmonic contributions to the dynamic stability of tetragonal $ZrO_2$. In our own DFT calculations this phase also appears after the distortion of a multilayer slab of tetragonal $ZrO_2(111)$. The metamonoclinic phase has a unit cell comprised of six atoms or two formula units. Figure 1(c) shows that this phase is derived from the tetragonal phase after a monoclinic distortion of its $c$ axis. The strong relationship with the monoclinic phase is also apparent as all Zr atoms are sevenfold coordinated and the atomic volume is only slightly smaller. Expansion of the monoclinic ground state structure, breaking two more bonds per unit cell in the process, leads to a second metastable structure, the anatase phase shown in Fig. 1(e). It consists of sixfold coordinated Zr atoms where each octahedron shares a corner with four neighboring octahedra, similar to the anatase phase of $TiO_2$. The octahedra are distorted such that two of the six Zr-O bonds are about 3.7% longer than the others. To our knowledge, there is no experimental evidence of this phase.

We determined the total energy of all five fully relaxed structures within the RPA framework (see Table I). The experimental order of stability of the monoclinic, tetragonal, and cubic phases is very well reproduced, and energy differences of 56 and 111 meV/f.u. for the tetragonal and cubic phases, respectively, are in very good agreement with the experimental enthalpy differences of 63 and 120 meV/f.u. at the respective phase transition temperatures which were extrapolated to $T = 0$ K in Ref [42] using the experimental values from [43]. The RPA also yields excellent agreement of the calculated lattice parameters at the respective equilibrium volumes for the monoclinic and tetragonal phases with the experimental parameters, which were extrapolated to $T = 0$ K using thermal expansion data [42,44], as shown in Table II. For the high-temperature cubic phase the simulations only show a slight underestimation of the predicted equilibrium volume. The anatase phase is strongly disfavored, with a difference of 206 meV/f.u. compared to the monoclinic ground state, and the metamonoclinic phase is disfavored by 10 meV/f.u. compared to the tetragonal phase. The values of the internal structural parameters are very well described, indicated by the underestimation of less than 2% for the height difference $d_z$ of the O planes in the tetragonal phase [see Fig. 1(b)].

To further verify our results we performed benchmark dMP2 and CCSD(T) total energy calculations on the structures yielded by the RPA calculations. In both cases, the same initial wave function generated by VASP was used. At the dMP2 level, we find only slight deviations in the calculated total energy differences for the tetragonal and cubic phases, also in good agreement with the DMC results discussed by Shin *et al.* [22]. On the other hand, the stability of the anatase phase is strongly decreased to 240 meV/f.u., and the predicted stability of the metamonoclinic phase is increased, leading to an exchange in the order of stability between the tetragonal and metamonoclinic phases. To investigate this discrepancy further, methods that truncate the many-body perturbation expansion of the electronic exchange and correlation energy at higher orders were used, in particular coupled cluster singles and doubles (CCSD) theory, and CCSD plus perturbative triples [CCSD(T)]. As indicated in Table I, the finite size corrected total energy differences agree to within 10–20 meV and show the same order of stabilities as the RPA results, validating the reliability of the computationally more efficient method for the present $ZrO_2$ phases. The dMP2 on the other hand does perform slightly worse, indicated by its predicted increased stability of the metamonoclinic phase. It should be noted that while coupled cluster calculations are often cited as reference methods, they still have to be well converged to yield reference values. In the present case we have to conclude that, while the precision of the calculated energies does conform to these constraints, the desired accuracy is still not completely reached due to the size of the $ZrO_2$ bulk system.

Finally, we evaluated the performance of various DFT functionals and methods that improve the description of the exchange or long-range interactions, like hybrid functionals and van der Waals corrections respectively, of the $ZrO_2$system. At the DFT level, the calculated total energy differences of the studied $ZrO_2$ phases reveal major shortcomings of the commonly used exchange-correlation functionals. While the LDA energies are in good agreement with the reference values, the structural properties are less well described (see Table II). The PBE functional at least reproduces correctly the order of stability of the cubic, tetragonal, and monoclinic phases. However, the stabilities of the metamonoclinic and the anatase phases are vastly overestimated, being just 49 and 23 meV less stable than the ground state respectively. We relate this result to the tendency of the PBE functional to overestimate bond lengths and the stability of open structures. Adding van der Waals corrections using Grimme's D3 approach decreases the relative stability of the high-volume anatase phase, shifting it close to the

TABLE II. $ZrO_2$ equilibrium lattice parameters evaluated with various functionals. The bulk modulus $B_0$ was determined from a fit to the Birch-Murnaghan equation of state. The experimental lattice constants were extrapolated to zero temperature according to Aldebert *et al.* [44] and $B_0$ values were obtained at room temperature.

| | LDA | PBE | PBE-D3 | SCAN | SCAN-rVV10 | HSE06 | HSE06-D3 | RPA | DMC [22] | Expt. |
|---|---|---|---|---|---|---|---|---|---|---|
| | | | | | | cubic | | | | |
| $V$ (Å$^3$) | 31.84 | 33.52 | 33.09 | 32.96 | 32.84 | 32.62 | 32.16 | 32.03 | 32.60 | 32.97[a] |
| $B_0$ (GPa) | 268 | 235 | 239 | 259 | 262 | 262 | 267 | 253 | 278 | 194[b] |
| | | | | | | tetragonal | | | | |
| $c/a$ | 1.436 | 1.459 | 1.454 | 1.455 | 1.449 | 1.449 | 1.445 | 1.446 | 1.443 | 1.451 |
| $d_z$ | 0.042 | 0.057 | 0.054 | 0.054 | 0.050 | 0.052 | 0.049 | 0.046 | 0.047 | 0.047 |
| $V$ (Å$^3$) | 32.30 | 34.69 | 34.10 | 33.89 | 33.70 | 33.52 | 32.94 | 33.37 | 33.29 | 33.01[a] |
| $B_0$ (GPa) | 202 | 150 | 158 | 179 | 185 | 178 | 187 | 199 | 265 | 152[c]–198[d] |
| | | | | | | metamonoclinic | | | | |
| $b/a$ | 0.900 | 0.908 | 0.903 | 0.913 | 0.913 | 0.907 | 0.903 | 0.908 | | |
| $c/a$ | 1.405 | 1.416 | 1.412 | 1.419 | 1.417 | 1.413 | 1.410 | 1.417 | | |
| $\beta$ (deg) | 75.74 | 75.92 | 75.90 | 76.85 | 77.38 | 76.02 | 76.10 | 76.00 | | |
| $V$ (Å$^3$) | 34.12 | 36.21 | 35.58 | 35.45 | 35.21 | 35.14 | 34.53 | 35.13 | | |
| $B_0$ (GPa) | 172 | 144 | 157 | 154 | 159 | 165 | 192 | 193 | | |
| | | | | | | monoclinic | | | | |
| $b/a$ | 1.019 | 1.010 | 1.014 | 1.015 | 1.018 | 1.011 | 1.013 | 1.009 | 1.012 | 1.012 |
| $c/a$ | 1.030 | 1.037 | 1.036 | 1.037 | 1.035 | 1.033 | 1.034 | 1.037 | 1.031 | 1.032 |
| $\beta$ (deg) | 99.48 | 99.64 | 99.71 | 99.31 | 99.23 | 99.55 | 99.58 | 99.67 | 99.23 | 99.23 |
| $V$ (Å$^3$) | 34.10 | 36.10 | 35.59 | 35.32 | 35.08 | 35.17 | 34.62 | 35.16 | 34.98 | 35.22[e] |
| $B_0$ (GPa) | 189 | 159 | 158 | 163 | 160 | 180 | 178 | 229 | 254 | 201[f]–212[g] |
| | | | | | | anatase | | | | |
| $c/a$ | 1.064 | 1.066 | 1.061 | 1.066 | 1.064 | 1.066 | 1.059 | 1.060 | | |
| $\beta$ (deg) | 117.66 | 117.61 | 117.75 | 117.33 | 117.39 | 117.73 | 117.76 | 117.76 | | |
| $V$ (Å$^3$) | 41.83 | 43.78 | 43.26 | 43.05 | 42.91 | 42.76 | 42.19 | 42.82 | | |
| $B_0$ (GPa) | 190 | 170 | 171 | 184 | 185 | 178 | 178 | 189 | | |

[a]Reference [42].
[b]Reference [47].
[c]Reference [52].
[d]Reference [49].
[e]Reference [54].
[f]Reference [53].
[g]Reference [50].

tetragonal phase. Interestingly, while the hybrid HSE06 functional clearly improves the description of the electronic properties, it still predicts a higher stability of both the metamonoclinic and the anatase phase compared to the tetragonal phase. While the latter issue can be partially improved by adding DFT-D3 van der Waals corrections, the relative stability of the metamonoclinic phase remains nearly unchanged. For the DFT functionals, we find the best performance using the recently developed SCAN metaGGA functional. Here, the stability of the cubic and tetragonal phases is greatly enhanced, reducing the difference between the tetragonal and metamonoclinic phases to 11 meV. Additionally, the anatase phase is shifted close to the cubic phase. This is a consequence of the improved treatment of intermediate van der Waals interactions in SCAN compared to PBE and HSE06 [30]. Finally, the additional treatment of long-range dispersion effects in the SCAN-rVV10 functional yields a further stabilization of the cubic and tetragonal phases, with the latter now being more stable than the metamonoclinic phase. Also, the predicted relative stability of the anatase phase is found to be much lower compared to the cubic phase.

While the SCAN metaGGA yields significant improvements in the predicted phase stabilities, electronic properties like the band gap are still not well described. As shown in Table III, the band gap for most phases widens by about 0.5 eV for the SCAN and about 1.6 eV for the hybrid HSE06 functional compared to PBE, except for the monoclinic phase. There, the improvements upon the PBE functional are only 0.06 and 1.24 eV for SCAN and HSE06, respectively. This issue is only alleviated with $G_0W_0$ calculations at the RPA level of theory where our calculated values of 5.6 eV for the monoclinic phase agree well with Jiang *et al.* [45]. Band gaps calculated with the van der Waals corrected functionals do

TABLE III. Band gaps in units of eV for the presented $ZrO_2$ phases evaluated at the respective equilibrium volumes.

| Band gap (eV) | PBE | SCAN | HSE06 | $G_0W_0$ | $G_0W_0$ [45] | Expt. [1] |
|---|---|---|---|---|---|---|
| cubic | 3.37 | 3.86 | 5.03 | 4.87 | 4.62 | |
| tetragonal | 4.13 | 4.63 | 5.75 | 5.74 | 5.56 | |
| monoclinic | 4.06 | 4.13 | 5.29 | 5.61 | 4.99 | >5.8 |
| metamonoclinic | 4.27 | 4.79 | 5.95 | 5.95 | | |
| anatase | 3.99 | 4.50 | 5.59 | 5.76 | | |

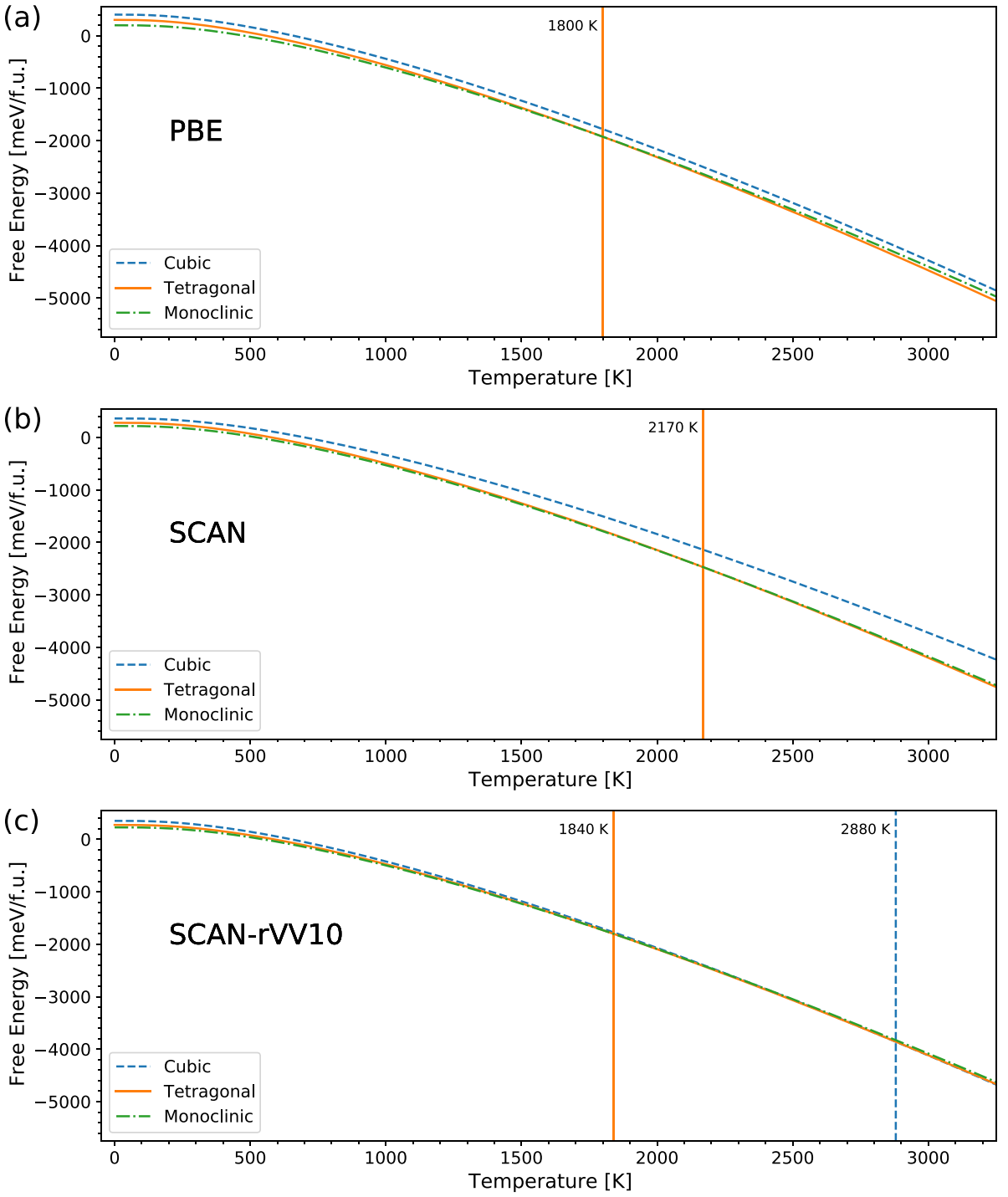


FIG. 2. Helmholtz free energy $F(T)$ in the harmonic approximation calculated with the (a) PBE, (b) SCAN, and (c) SCAN-rVV10 functionals. The crossing points highlighted by horizontal lines indicate the predicted monoclinic-tetragonal and tetragonal-cubic phase transition temperatures.

not lead to significantly different results and are included in Supplemental Material Table S-IV [46].

To further evaluate the performance of the used methods we computed the elastic constants and Voight bulk modulus $B_v$ for the cubic, tetragonal, and monoclinic phases. Since the evaluation of the stress tensor for RPA calculations is not yet implemented in VASP, this was only done with selected GGA and metaGGA functionals. Where applicable, the Voight bulk modulus was related to the value of $B_0$ extracted from the fit to the Birch-Murnaghan equation of state, with a significantly smaller deviation from experimental values compared to the diffusion MC results reported by Shin *et al.* [22]. All calculated values are tabulated in Supplemental Material Table S-III. It should also be noted that experimental values often suffer from large error bars. Room temperature measurements of the elastic constants of cubic $ZrO_2$ performed

TABLE IV. Zero-point vibrational energy corrections referenced to the monoclinic phase in meV per formula unit.

| | c | t | meta | m | a |
|---|---|---|---|---|---|
| | | | (meV/formula unit) | | |
| ZPVE correction | | | | | |
| PBE | −10 | −6 | +3 | 0 | −6 |
| SCAN | −16 | −5 | −6 | 0 | +9 |
| SCAN-rVV10 | −13 | −5 | +14 | 0 | +2 |
| RPA | +8 | +6 | +9 | 0 | −8 |
| ZPVE corrected total energy differences | | | | | |
| PBE | 203 | 103 | 52 | 0 | 17 |
| SCAN | 143 | 61 | 49 | 0 | 169 |
| SCAN-rVV10 | 124 | 47 | 70 | 0 | 219 |
| RPA | 119 | 62 | 75 | 0 | 198 |

by Kandil *et al.* [47] were done with a 8.1 mol % $Y_2O_3$ Yttrium-stabilized crystal and the final values were extrapolated at room temperature to 0 mol % $Y_2O_3$, yielding $C_{11} = 417$ GPa, $C_{12} = 82$ GPa, and $C_{44} = 47$ GPa. Extrapolation of their published experimental data with higher $Y_2O_3$ content using the formula suggested by Varshni [48] describing the temperature dependence of elastic stiffness coefficients shows that the values at room temperature are already very close to those at $T = 0$ K [46]. We assume similar behavior for pure cubic $ZrO_2$. For the tetragonal and monoclinic phases the problem of stabilizing the crystal at the desired temperature is slightly alleviated, but published values of the bulk modulus measured at room temperature still range from 201 [49] to 212 GPa [50] for the monoclinic phase, depending on the amount of experimental noise and whether the compressibility was determined from the second-order equation of state or from the elastic tensor. We also assume that in these cases the values at $T = 0$ K should again be very close to the room temperature measurements.

According to our evaluation, for the cubic $ZrO_2$ phase all functionals yield a substantial overestimation of the Voight bulk modulus $B_v$ of between 41 and 149 GPa for the PBE and SCAN functionals, respectively, compared to the experimental values. The minuscule differences of the PBE and PBE-D3 results can be attributed to the slight differences of their respective equilibrium volumes and are very similar to the results recently reported by Delarmelina *et al.* [51]. The van der Waals corrected SCAN-rVV10 functional on the other hand greatly improves on the pure SCAN results for the individual elastic constants $C_{11}$, $C_{12}$, and $C_{44}$, yielding the most uniform difference compared to the experiment. Due to the aforementioned technical constraints the predicted compressibility for the RPA method is only available from the fit to the Birch-Murnaghan equation of state, yielding an overestimation of $B_0$ of 59 GPa.

For the tetragonal phase the SCAN functional yields the largest deviation of the individual elastic constants from the experimental results reported by Kisi *et al.* [52], leading to a large overestimation of the bulk modulus. A more recent work by Bouvier *et al.* [49] reports much lower compressibility of the undoped tetragonal $ZrO_2$ crystal and a bulk modulus of 198 GPa, leading to much better agreement of our calculated bulk modulus. The comparison of the reported $B_0 = 172$ GPa calculated from the equation of state agrees very well with our SCAN results derived using the same method, as shown in Table III. Both SCAN-rVV10 and the RPA yield larger values, while PBE and PBE-D3 result in an underestimation of the bulk modulus.

Finally, for the monoclinic phase both SCAN and SCAN-rVV10 yield very good agreement of the individual elastic constants with the experimental values reported by Chan *et al.* [53] compared to the other functionals. Still, the average aberration from the experimental values is larger than for the cubic and tetragonal phases. The predicted bulk modulus calculated in the Voight approximation is overestimated for both functionals, while PBE and PBE-D3 yield very good agreement. Comparing the bulk modulus extracted from the second-order equation of state shows a significant underestimation of $B_0$ compared to Desgreniers *et al.* [50], with the best prediction yielded by the RPA.

Relating the DFT results to our RPA calculations shows that using a hybrid approach like HSE06, which provides an improved description of exchange effects and correspondingly the electronic structure, only yields a small improvement of the $ZrO_2$ bulk stabilities compared to the benchmark. The predicted high stability of the anatase phase for both the PBE and the hybrid functionals indicates that a proper description of long range effects plays a decisive role, greatly reducing its predicted stability for the PBE-D3 and HSE06-D3 functionals. Both PBE and HSE06 also predict a too high stability of the metamonoclinic $ZrO_2$ bulk phase, irrespective of whether or not van der Waals corrections were applied. The SCAN metaGGA on the other hand yields a much improved description of the structural parameters of the $ZrO_2$ system. The predicted stability of the cubic and anatase phases are still under- and overestimated with the "pure" SCAN functional, respectively. Both tetragonal and metamonoclinic phase stabilities are close to the RPA values, but the order of stability is still wrong. Only after including a proper treatment of both short- and long-range van der Waals interactions within the SCAN-rVV10 functional did the predicted order of stability agree with the RPA and coupled cluster benchmark values.

Finally, we also computed the Helmholtz free energy $F(T)$ to investigate the contributions of the zero-point vibrational energies (ZPVE) to energetic differences between the respective phases with the PBE and SCAN functionals and with the RPA. The ZPVEs were calculated as the sum over the vibrational density of states (DOS) using the PHONOPY package [37] at the equilibrium volume of the particular $ZrO_2$ phase. The calculations were performed on $3 \times 3 \times 3$ model cells involving 108 formula units per model cell for the DFT and $2 \times 2 \times 2$ model cells with 32 formula units per model cell for the RPA calculations, respectively. Due to the worse scaling behavior of the RPA method the limitations of computational power did not allow us to perform the simulations on larger unit cells.

As indicated in Table IV the large error bar of the bulk modulus in the DFT framework is also reflected in the relative zero-point energy correction: while we generally find values of up to 16 meV, the PBE, SCAN, and SCAN-rVV10 functionals predict the wrong sign for the difference between the cubic/tetragonal and the monoclinic phase. For the

competition between the tetragonal and the metamonoclinic phases we find only a minor influence of the ZPVE corrections: even though the PBE functional overestimates the stabilization of the tetragonal phase (9 meV compared to the RPA value of 3 meV), the PBE total energy differences (see Table I) are much larger, and the ZPVE corrections do not change the order of stability. This differs for the metaGGA: while the pure SCAN functional shifts both tetragonal and metamonoclinic phases in the same direction, the van der Waals corrected SCAN-rVV10 results in a decrease of the stability of the metamonoclinic phase by 19 meV with respect to the tetragonal phase. The ZPVE calculated in the RPA within the smaller $2 \times 2 \times 2$ model cell yields an increase of the stability of the monoclinic ground state phase, but has little impact on the relative order of stability of the high-temperature phases. Taking only the ZPVE corrections into account, the comparison with the experimental enthalpy differences at the phase transition temperature already shows excellent agreement of the RPA total energy differences.

To quantify the validity of the harmonic approximation we used the free energy $F(T)$ to determine the transition temperature from the monoclinic ground state first to the tetragonal and finally to the cubic phase, predicted by the various functionals. Generally, the accuracy of the harmonic approximation depends on two factors. In the present case, Souvatzis *et al.* [55] have shown that anharmonic effects play a significant role in the stability of the cubic phase, leading to significant errors of the predicted tetragonal-cubic transition temperature in the harmonic approximation. Also, the accuracy of the harmonic approximation depends on a well converged supercell size, which is usually limited by the available computational resources. As shown in Fig. 2, for the studied $ZrO_2$ phases, we find that the PBE, SCAN, and SCAN-rVV10 functionals predict an onset temperature of 1800, 2170, and 1840 K for the first phase transition from the monoclinic to the tetragonal phase, a significant overestimation of the experimental value of 1270–1370 K. The phase transition from the tetragonal to the cubic phase is only predicted by the SCAN-rVV10 functional at 2880 K, surprisingly close to the experimental value of 2650 K, while all other functionals do not yield a crossing point of the respective Helmholtz free energy $F(T)$ functions. For the RPA we do not find a crossing of the free energy curves for both phase transitions. Due to the glancing intersection of the free energy curves (see Fig. 2), this might be related to the lesser convergence of calculated phonon spectra in the smaller $2 \times 2 \times 2$ unit cells. On the other hand, the missing crossing points of the free energy curves at the RPA level might also suggest an increased importance of anharmonic contributions. This would also imply that the agreement of commonly used DFT functionals in the harmonic approximation seems to be the result of fortuitous cancellation of errors.

## IV. CONCLUSIONS

To summarize, we present a thorough examination of the performance of DFT and beyond-DFT methods concerning the reproduction of the complex phase diagram of stoichiometric $ZrO_2$. We have shown that the commonly used DFT exchange-correlation functionals vastly overestimate the stability of the metamonoclinic and anatase phases and also yield too large energy differences for the well known tetragonal and cubic phases with respect to the monoclinic ground state. Our results show that hybrid functionals (HSE06) offer only small improvement of the $ZrO_2$ phase stabilities, but adding van der Waals corrections (e.g., by Grimme's D3 approach) decreases the error for the high-volume anatase phase. Methods which augment standard DFT like correlated approaches offer a significant improvement of the predicted phase stabilities, albeit at a significantly higher computational cost. In addition, we find that the metaGGA type SCAN-rVV10 functional is an excellent compromise as it provides results which are often close to the many-electron reference calculations and to the experimental values, which allows the simulation of much larger systems than with a correlated method at comparable accuracy.

## ACKNOWLEDGMENTS

We thank Prof. Georg Kresse (University of Vienna) for fruitful discussions and insightful comments. This work was supported by the Austrian Science Fund (FWF project F45 "FOXSI") and the Vienna Scientific Cluster (VSC). The structural models were created with the program VESTA [56].

[1] R. H. French, S. J. Glass, F. S. Ohuchi, Y. N. Xu, and W. Y. Ching, Experimental and theoretical determination of the electronic structure and optical properties of three phases of $ZrO_2$, Phys. Rev. B **49**, 5133 (1994).

[2] E. H. Kisi and C. Howard, Crystal structures of zirconia phases and their inter-relation, Key Eng. Mater. **153-154**, 1 (1998).

[3] T. S. Böscke, J. Müller, D. Bräuhaus, U. Schröder, and U. Böttger, Ferroelectricity in hafnium oxide thin films, Appl. Phys. Lett. **99**, 102903 (2011).

[4] J. Müller, T. S. Böscke, D. Bräuhaus, U. Schröder, U. Böttger, J. Sundqvist, P. Kücher, T. Mikolajick, and L. Frey, Ferroelectric $Hf_{0.5}Zr_{0.5}O_2$ thin films for nonvolatile memory applications, Appl. Phys. Lett. **99**, 112901 (2011).

[5] Y. Wei, P. Nukala, M. Salverda, S. Matzen, H. J. Zhao, J. Momand, A. S. Everhardt, G. Agnus, G. R. Blake, P. Lecoeur, B. J. Kooi, J. Íñiguez, B. Dkhil, and B. Noheda, A rhombohedral ferroelectric phase in epitaxially strained $Hf_{0.5}Zr_{0.5}O_2$ thin films, Nat. Mater. **17**, 1095 (2018).

[6] R. Materlik, C. Künneth, and A. Kersch, The origin of ferroelectricity in $Hf_{0.5}Zr_{0.5}O_2$: A computational investigation and a surface energy model, J. Appl. Phys. **117**, 134109 (2015).

[7] J. D. McCullough and K. N. Trueblood, The crystal structure of baddeleyite (monoclinic $ZrO_2$), Acta Crystallogr. **12**, 507 (1959).

[8] J. Wang, H. P. Li, and R. Stevens, Hafnia and hafnia-toughened ceramics, J. Mater. Sci. **27**, 5397 (1992).

[9] X. Luo, W. Zhou, S. V. Ushakov, A. Navrotsky, and A. A. Demkov, Monoclinic to tetragonal transformations in hafnia

and zirconia: A combined calorimetric and density functional study, Phys. Rev. B **80**, 134119 (2009).
[10] J. M. Leger, P. E. Tomaszewski, A. Atouf, and A. S. Pereira, Pressure-induced structural phase transitions in zirconia under high pressure, Phys. Rev. B **47**, 14075 (1993).
[11] Y. Al-Khatatbeh, K. K. M. Lee, and B. Kiefer, Phase relations and hardness trends of $ZrO_2$ phases at high pressure, Phys. Rev. B **81**, 214102 (2010).
[12] E. H. Kisi, C. J. Howard, and R. J. Hill, Crystal structure of orthorhombic zirconia in partially stabilized zirconia, J. Am. Ceram. Soc. **72**, 1757 (1989).
[13] M. Antlanger, W. Mayr-Schmölzer, J. Pavelec, F. Mittendorfer, J. Redinger, P. Varga, U. Diebold, and M. Schmid, $Pt_3Zr(0001)$: A substrate for growing well-ordered ultrathin zirconia films by oxidation, Phys. Rev. B **86**, 035451 (2012).
[14] H. Li, J.-I. J. Choi, W. Mayr-Schmölzer, C. Weilach, C. Rameshan, F. Mittendorfer, J. Redinger, M. Schmid, and G. Rupprechter, Growth of an ultrathin zirconia film on $Pt_3Zr$ examined by high-resolution x-ray photoelectron spectroscopy, temperature-programmed desorption, scanning tunneling microscopy, and density functional theory, J. Phys. Chem. C **119**, 2462 (2015).
[15] P. Lackner, J. I. J. Choi, U. Diebold, and M. Schmid, Substoichiometric ultrathin zirconia films cause strong metal-support interaction, J. Mater. Chem. A **7**, 24837 (2019).
[16] J. I. J. Choi, W. Mayr-Schmölzer, F. Mittendorfer, J. Redinger, U. Diebold, and M. Schmid, The growth of ultra-thin zirconia films on $Pd_3Zr(0001)$, J. Phys.: Condens. Matter **26**, 225003 (2014).
[17] J. K. Dewhurst and J. E. Lowther, Relative stability, structure, and elastic properties of several phases of pure zirconia, Phys. Rev. B **57**, 741 (1998).
[18] C. Ricca, A. Ringuedé, M. Cassir, C. Adamo, and F. Labat, A comprehensive DFT investigation of bulk and low-index surfaces of $ZrO_2$ polymorphs, J. Comput. Chem. **36**, 9 (2015).
[19] J. C. Thomas and A. Van der Ven, Order parameters for symmetry-breaking structural transitions: The tetragonal-monoclinic transition in $ZrO_2$, Phys. Rev. B **96**, 134121 (2017).
[20] S. H. Guan, X. J. Zhang, and Z. P. Liu, Energy landscape of zirconia phase transitions, J. Am. Chem. Soc. **137**, 8010 (2015).
[21] M.-H. Chen, J. C. Thomas, A. R. Natarajan, and A. Van der Ven, Effects of strain on the stability of tetragonal $ZrO_2$, Phys. Rev. B **94**, 054108 (2016).
[22] H. Shin, A. Benali, Y. Luo, E. Crabb, A. Lopez-Bezanilla, L. E. Ratcliff, A. M. Jokisaari, and O. Heinonen, Zirconia and hafnia polymorphs: Ground-state structural properties from diffusion Monte Carlo, Phys. Rev. Mater. **2**, 075001 (2018).
[23] K. Lejaeghere, G. Bihlmayer, T. Björkman, P. Blaha, S. Blügel, V. Blum, D. Caliste, I. E. Castelli, S. J. Clark, A. Dal Corso, S. de Gironcoli, T. Deutsch, J. K. Dewhurst, I. Di Marco, C. Draxl, M. Dułak, O. Eriksson, J. A. Flores-Livas, K. F. Garrity, *et al.*, Reproducibility in density functional theory calculations of solids, Science **351**, aad3000 (2016).
[24] G. Kresse and D. Joubert, From ultrasoft pseudopotentials to the projector augmented-wave method, Phys. Rev. B **59**, 1758 (1999).
[25] J. P. Perdew, K. Burke, and M. Ernzerhof, Generalized Gradient Approximation Made Simple, Phys. Rev. Lett. **77**, 3865 (1996).
[26] J. Sun, A. Ruzsinszky, and J. P. Perdew, Strongly Constrained and Appropriately Normed Semilocal Density Functional, Phys. Rev. Lett. **115**, 036402 (2015).
[27] A. V. Krukau, O. A. Vydrov, A. F. Izmaylov, and G. E. Scuseria, Influence of the exchange screening parameter on the performance of screened hybrid functionals, J. Chem. Phys. **125**, 224106 (2006).
[28] S. Grimme, J. Antony, S. Ehrlich, and H. Krieg, A consistent and accurate ab initio parametrization of density functional dispersion correction (DFT-D) for the 94 elements H-Pu, J. Chem. Phys. **132**, 154104 (2010).
[29] R. Sabatini, T. Gorni, and S. de Gironcoli, Nonlocal van der Waals density functional made simple and efficient, Phys. Rev. B **87**, 041108(R) (2013).
[30] H. Peng, Z.-H. Yang, J. P. Perdew, and J. Sun, Versatile van der Waals Density Functional Based on a Meta-Generalized Gradient Approximation, Phys. Rev. X **6**, 041005 (2016).
[31] R. Ahuja, A. Blomqvist, P. Larsson, P. Pyykkö, and P. Zaleski-Ejgierd, Relativity and the Lead-Acid Battery, Phys. Rev. Lett. **106**, 018301 (2011).
[32] P. Pyykkö, Relativistic Effects in chemistry: More common than you thought, Annu. Rev. Phys. Chem. **63**, 45 (2012).
[33] M. Kaltak, J. Klimeš, and G. Kresse, Cubic scaling algorithm for the random phase approximation: Self-interstitials and vacancies in Si, Phys. Rev. B **90**, 054115 (2014).
[34] B. Ramberger, T. Schäfer, and G. Kresse, Analytic Interatomic Forces in the Random Phase Approximation, Phys. Rev. Lett. **118**, 106403 (2017).
[35] F. Birch, Finite elastic strain of cubic crystals, Phys. Rev. **71**, 809 (1947).
[36] Y. Le Page and P. Saxe, Symmetry-general least-squares extraction of elastic data for strained materials from *ab initio* calculations of stress, Phys. Rev. B **65**, 104104 (2002).
[37] A. Togo and I. Tanaka, First principles phonon calculations in materials science, Scr. Mater. **108**, 1 (2015).
[38] F. Hummel, T. Tsatsoulis, and A. Grüneis, Low rank factorization of the Coulomb integrals for periodic coupled cluster theory, J. Chem. Phys. **146**, 124105 (2017).
[39] E. Solomonik, D. Matthews, J. R. Hammond, J. F. Stanton, and J. Demmel, A massively parallel tensor contraction framework for coupled-cluster computations, J. Parallel Distrib. Comput. **74**, 3176 (2014).
[40] A. Grüneis, G. H. Booth, M. Marsman, J. Spencer, A. Alavi, and G. Kresse, Natural orbitals for wave function based correlated calculations using a plane wave basis set, J. Chem. Theory Comput. **7**, 2780 (2011).
[41] T. Gruber, K. Liao, T. Tsatsoulis, F. Hummel, and A. Grüneis, Applying the Coupled-Cluster Ansatz to Solids and Surfaces in the Thermodynamic Limit, Phys. Rev. X **8**, 021043 (2018).
[42] E. V. Stefanovich, A. L. Shluger, and C. R. A. Catlow, Theoretical study of the stabilization of cubic-phase $ZrO_2$ by impurities, Phys. Rev. B **49**, 11560 (1994).
[43] R. Ackermann, E. Rauh, and C. Alexander, The thermodynamic properties of $ZrO_2$(g), High Temp. Sci **7**, 304 (1975).
[44] P. Aldebert and J.-P. Traverse, Structure and ionic mobility of zirconia at high temperature, J. Am. Ceram. Soc. **68**, 34 (1985).
[45] H. Jiang, R. I. Gomez-Abal, P. Rinke, and M. Scheffler, Electronic band structure of zirconia and hafnia polymorphs from the *GW* perspective, Phys. Rev. B **81**, 085119 (2010).

[46] See Supplemental Material at http://link.aps.org/supplemental/10.1103/PhysRevResearch.2.043361 for a detailed description of the method used to model the temperature dependence of the measured elastic constants of $ZrO_2$.

[47] H. M. Kandil, J. D. Greiner, and J. F. Smith, Single-crystal elastic constants of yttria-stabilized zirconia in the range 20° to 700°C, J. Am. Ceram. Soc. **67**, 341 (1984).

[48] Y. P. Varshni, Temperature dependence of the elastic constants, Phys. Rev. B **2**, 3952 (1970).

[49] P. Bouvier, E. Djurado, G. Lucazeau, and T. Le Bihan, High-pressure structural evolution of undoped tetragonal nanocrystalline zirconia, Phys. Rev. B **62**, 8731 (2000).

[50] S. Desgreniers and K. Lagarec, High-density $ZrO_2$ and $HfO_2$: Crystalline structures and equations of state, Phys. Rev. B **59**, 8467 (1999).

[51] M. Delarmelina, M. G. Quesne, and C. R. A. Catlow, Modelling the bulk properties of ambient pressure polymorphs of zirconia, Phys. Chem. Chem. Phys. **22**, 6660 (2020).

[52] E. H. Kisi and C. J. Howard, Elastic constants of tetragonal zirconia measured by a new powder diffraction technique, J. Am. Ceram. Soc. **81**, 1682 (2005).

[53] S.-K. Chan, Y. Fang, M. Grimsditch, Z. Li, M. V. Nevitt, W. M. Robertson, and E. S. Zouboulis, Temperature dependence of the elastic moduli of monoclinic zirconia, J. Am. Ceram. Soc. **74**, 1742 (1991).

[54] C. J. Howard, R. J. Hill, and B. E. Reichert, Structures of $ZrO_2$ polymorphs at room temperature by high-resolution neutron powder diffraction, Acta Crystallogr. Sect. B Struct. Sci. **44**, 116 (1988).

[55] P. Souvatzis and S. P. Rudin, Dynamical stabilization of cubic $ZrO_2$ by phonon-phonon interactions: *Ab initio* calculations, Phys. Rev. B **78**, 184304 (2008).

[56] K. Momma and F. Izumi, VESTA 3 for three-dimensional visualization of crystal, volumetric and morphology data, J. Appl. Crystallogr. **44**, 1272 (2011).